Supporting Information

Spacer Ligands Enhance Mn-Dopant Luminescence *via* Tailored Exciton Dynamics in 2D Ruddlesden-Popper Perovskites

*Amar Nath Yadav[1], Du Chen[2, 3], Idan Karev[4], Shunran Li[2, 3], Jee Yung Park[2, 3], Daphna Shimon[4], Mikaël Kepenekian[5], Peijun Guo[2, 3], Ido Hadar[1]**

[1]*Institute of Chemistry, the Center for Nanoscience and Nanotechnology, and Casali Center for Applied Chemistry, the Hebrew University of Jerusalem, Jerusalem 9190401, Israel.*

[2] *Department of Chemical and Environmental Engineering, Yale University, New Haven, CT 06520, USA.*

[3]*Energy Sciences Institute, Yale University, West Haven, Connecticut 06516, USA.*

[4]*Institute of Chemistry, the Hebrew University of Jerusalem, Jerusalem 9190401, Israel.*

[5]*Univ Rennes, ENSCR, INSA Rennes, CNRS, ISCR (Institut des Sciences Chimiques de Rennes), UMR 6226, Rennes F-35000, France*

*Corresponding author email: ido.hadar@mail.huji.ac.il

This supporting information includes:

Section 1: Experimental section

S1. Materials

Phenethylamine (99%, Thermo Fisher), butylamine (99%, Holland Morran), benzylamine (99%, thermo fisher), hexylamine (99%, Alfa Aesar), lead bromide ($PbBr_2$, 98%, Thermo Scientific), lead oxide (PbO, 99.9%, Alfa Aesar), manganese bromide, hydrobromic acid (HBr, 48%, Thermo Fisher), hypophosphorous acid (H_3PO_2, Thermo Fisher). The chemicals were used as received, without any additional purification.

S2. Synthesis

S2.1 Synthesis of undoped and Mn-doped $(BA)_2PbBr_4$ perovskite crystals

The undoped and Mn-doped L_2PbBr_4 (L = PEA or BA) crystals were synthesized using the acid precipitation method, as previously reported.[1,2] For the typical synthesis of $(BA)_2Pb_{1-x}Mn_xBr_4$ ($x_{Mn,\ feed}$ = 0.5), PbO (2.5 mmol, 0.5580 g) and $MnBr_2$ (2.5 mmol, 0.5368 g) were added to 5 mL of HBr and 0.85 mL of H_3PO_2. The mixture was heated to 90°C under stirring until a clear solution was obtained. Meanwhile, 988 µL (10 mmol) of butylamine was added dropwise to 5 mL of HBr in a separate vial under an ice bath. This butylamine mixture was then added dropwise to the above salt-precursor solution. The temperature was subsequently increased from 130°C to 150°C to dissolve the resulting precipitate. The mixture was then slowly cooled to room temperature without further disturbance. During cooling, crystals were precipitated, washed with acetone, and vacuum-dried. Similarly, other crystals of $(BA)_2Pb_{1-x}Mn_xBr_4$ ($x_{Mn,\ feed}$ = 0, 0.70, 0.90) were synthesized using the same procedure.

S2.3 Synthesis of undoped and Mn-doped $(PEA)_2PbBr_4$ perovskite crystals

For the synthesis of $(PEA)_2Pb_{1-x}Mn_xBr_4$ ($x_{Mn,\ feed}$ = 0–0.90) crystals, the same method was followed, with the only difference being that phenethylamine (200 µL) was added dropwise directly to the solution containing PbO, $MnBr_2$, HBr, and H_3PO_2, instead of being pre-mixed in HBr.

S2.4 Synthesis of undoped and Mn-doped $(BzA)_2PbBr_4$ perovskite crystals

For the synthesis of $(BzA)_2Pb_{1-x}Mn_xBr_4$ ($x_{Mn,\ feed}$ = 0.90) crystals, 0.25 mmol (0.0558 g) of PbO and 2.25 mmol (0.4831g) of $MnBr_2$ were dissolved in 10 ml of HBr at 90°C under magnetic stirring. Further, in another vial, 100 µL of benzylamine and 0.425 mL of H_3PO_2 were mixed. This benzylamine mixture was then added dropwise to the above salt-precursor solution. The

temperature was increased to 160°C and held at that temperature until the precipitate dissolved. Further, the temperature was decreased very slowly to room temperature. The obtained crystals were dried under vacuum and washed several times with acetone.

S2.5 Synthesis of undoped and Mn-doped $(HA)_2PbBr_4$ perovskite crystals

For the synthesis of $(HA)_2Pb_{1-x}Mn_xBr_4$ ($x_{Mn,\ feed}$ = 0.90) crystals, 0.25 mmol (0.0558 g) of PbO and 2.25 mmol (0.4831g) of $MnBr_2$ were dissolved in 10 ml of HBr at 90°C under magnetic stirring. Further 5 mmol (389 µL) of hexylamine and 0.85 ml of H_3PO_2 were mixed together. This hexylamine mixture was then added dropwise to the above salt-precursor solution. The temperature was increased to 160°C to dissolve the obtained precipitate. Furthermore, the temperature was decreased from 160°C to 100°C and from 100°C to 25°C at rates of 10°C/h and 1°C/h, respectively, to obtain high-quality crystals. The obtained crystals were dried under reduced pressure and washed several times with acetone.

S3. Characterizations

S3.1 Optical characterizations

The UV-Vis absorption and photoluminescence (PL) spectra were measured using a UV-Vis-NIR JASCO spectrophotometer and a PL-RF6000 fluorescence spectrometer, respectively. In absorption spectroscopy, the reflection from the crystals was measured and converted to absorbance. Low-temperature PL spectra were recorded on a home-built micro-spectroscopy setup. A laser with a wavelength of 371 nm and a repetition rate of 10 MHz was used to excite the samples. PL quantum yield (PLQY) measurements were conducted on the Edinburgh Instruments FS5 v2 spectrofluorometer. An excitation wavelength of 375 nm was used for PLQY measurements in all samples.

Raman spectroscopy was performed using a customized microscope-coupled spectrometer setup. A long working-distance objective lens (Mitutoyo, NIR, 20×, NA = 0.4) was employed to focus the 785 nm excitation light generated by a frequency-stabilized laser (Toptica) onto the sample. The resulting inelastically scattered Raman signal was collected with the same objective and filtered using a series of five narrow-bandwidth reflective volume Bragg grating notch filters (OptiGrate), enabling detection of Raman shifts as low as 5 cm^{-1}. The filtered signal was then directed through two 75 mm focal-length achromatic lenses and a 50 µm pinhole before entering

a spectrograph (Horiba iHR550, equipped with a 950 grooves/mm grating) and finally detected by a CCD camera (Horiba Syncerity).

Continuous wave (CW) electron paramagnetic resonance (EPR) measurements were recorded using a Bruker EMXplus spectrometer operated in the X-band (9.5 GHz). All the experiments were performed at room temperature. For low-doped samples, an attenuation of 5 dB was applied to achieve a high signal-to-noise ratio. Fitting of the experimental EPR spectra was performed using EasySpin.

Time-resolved PL decay measurements were performed using an Edinburgh Instruments FS5 v2 spectrofluorometer. The samples were excited with a 370 nm laser operating at a repetition rate of 5 MHz. A 395 nm long-pass filter was placed in front of the detector to suppress scattered excitation photons.

S3.2 Structural characterizations

X-ray diffraction (XRD) patterns were recorded on a Bruker AXS D8 Advance X-ray powder diffractometer using Cu Kα radiation (λ = 1.5406 Å). Scanning electron microscope (SEM) images were recorded using the Extra-high-resolution scanning electron microscope Magellan 400L (Thermo Fisher Scientific). Inductively Coupled Plasma Mass Spectrometry (ICP-MS) was performed on the Agilent Technologies 8900 ICP-MS Triple Quad. For this measurement, the samples were diluted to the ppb level in an aqueous 1% HNO_3 solution. Differential scanning calorimetry (DSC) curves were measured on a simultaneous thermal analyzer –NETZSCH STA 449F3 instrument. The bulk crystals were heated under N_2 with a ramp rate of 10°C/min.

S3.3 Cathodoluminescence (CL) measurement

CL measurements in a SEM were carried out on an Analytical High-Resolution SEM Apreo 2S (Thermo Fisher Scientific). The instrument was equipped with a SPARC system for CL spectroscopy and mapping. In this setup, an electron beam (with an operating voltage of 10 kV and a beam current of 3.2-6.4 nA) is directed onto the sample surface through an opening in a parabolic mirror. The stage height is carefully adjusted to position the light-emitting region of the sample at the mirror's focal point. This alignment is typically optimized by maximizing the intensity and symmetry of the detected signal. The emitted light, collected by the mirror, is then

guided out of the SEM's vacuum environment and focused directly onto a light detector. The obtained data were analyzed with Odemis Viewer software (Delmic).

S3.4 Transient reflection microscopy (TRM) measurement for carrier diffusivity

A schematic illustration of our TRM setup is shown in **Figure S7A**. The pump light, centered at 640 nm, was generated using an optical parametric amplifier (OPA, Orpheus ONE) driven by a Pharos amplifier, which produces a fundamental output at 1030 nm with a pulse duration of 170 fs and a repetition rate of 2 kHz. A portion of this fundamental light was split and time-delayed using a mechanical delay stage, then focused onto a 4-mm-thick YAG crystal to generate broadband visible light. A bandpass (BP) filter centered at 575 nm with a 20 nm bandwidth was used to isolate near-monochromatic, off-resonance probe light.

Due to the UV spectral position of the 2D bromide perovskite exciton resonance and the poor performance of high-numerical-aperture objectives in this regime, the probe light (derived from a broadband YAG source) was selected below the bandgap to ensure an adequate signal-to-noise ratio. As demonstrated in recent literature, below-bandgap TRM effectively captures excited-state population dynamics.[3,4] In this regime, the reflection contrast at the sample/substrate interface is dominated by transient modulations in the real part of the dielectric function induced by the excited populations, rather than changes in the imaginary part probed directly at resonance.

A f = 300 mm wide-field lens (WFL) focused the probe beam onto the back aperture of the objective, enabling wide-field illumination over an area of approximately 16 μm. The pump and probe beams were combined using a 50/50 beam splitter (BS) and directed into a long-working-distance objective (Mitutoyo G Plan Apo 50x, NA = 0.50) with 3.5 mm of glass correction. The pump beam was focused to a spot with a full width at half maximum (FWHM) of ~1.4 μm and excited the sample *via* two-photon absorption. The reflected probe light was collected through the same objective and focused onto the charged metal–oxide semiconductor (CMOS) camera (PixeLINK PL-D753) using an f = 400 mm tube lens, providing a total magnification of 100x (**Figure S7B**). A 550–600 nm bandpass filter was placed in front of the CMOS camera to block the reflected pump light and PL from the sample. The transient reflectance, $\frac{\Delta R}{R} = \frac{R(t)-R(0)}{R(0)}$, was calculated at each camera pixel, where R (0) and R (*t*) are the reflectance values before and after pump excitation, respectively (**Figure S7C**). The presence of charge carriers induces contrast

in the microscopy image through interferometric scattering, with the scattered intensity being directly proportional to the excited-state population density.[3] All measurements were performed at ambient temperature with the samples placed in a vacuum chamber.

The spatiotemporal distribution of charge carriers was extracted by azimuthally integrating the Gaussian-shaped contrast intensity in the imaging to obtain $I(r,t)$. Fitting a Gaussian distribution to $I(r,t)$ at each time point gives its standard deviation σ (**Figure S7D**). The mean-square-displacement (MSD) of the charge carriers can then be calculated as: $MSD(t) = \sigma(t)^2 - \sigma(0)^2$. A diffusive-to-sub-diffusive transport scheme was adopted here to account for the two subsequent diffusion regimes: 1) a normal diffusive regime with linear $MSD(t)$ behavior, i.e., $MSD(t) = 2Dt$, where D is the diffusivity; 2) a defect-mediated sub-diffusive regime with sublinear behavior, i.e., $MSD(t) = 2Dt^{\alpha}$, where $\alpha < 1$.[5] The measured $MSD(t)$ were then fitted with the following equation, which gives rise to diffusivity value:

$$MSD(t) = \begin{cases} 2Dt + c, & t \le t_{split} \\ 2D\left[\left(t - t_{split} + t_0\right)^{\alpha} + t_{split} - t_0^{\alpha}\right] + c, & t > t_{split} \end{cases}$$

where t_{split} is the separation point between the diffusive and sub-diffusive regimes, c is a small offset constant, α is the sub-diffusive exponent, and $t_0 = \alpha^{1/(1-\alpha)}$.[5]

The observed three-stage diffusion in Br-based perovskites, consisting of thermalization of hot carriers (<10 ps), followed by initial fast exciton diffusion regime (~10-150 ps) and slower exciton/heat diffusion regime (above ~150 ps), is consistent with literature on metals and semiconductors, where such behavior is similarly attributed to the diffusion of multiple carriers with distinct diffusivities and lifetimes.[6–9] The fast-diffusion regime is inaccessible via standard transient photoluminescence microscopy (TPLM), which has previously been used to study these materials, due to its limited time resolution and its sensitivity only to radiative excitons. Beyond this fast-diffusion regime, we extracted both diffusivity (faster and slower) values for $(PEA)_2PbI_4$, where slower diffusivity closely agrees with the values measured by TPLM (**Figure S10D**).

Theoretically, the coupled spatiotemporal evolution of these early-time processes can be fully quantified by solving the Two-Temperature Model (TTM) equations:[6,7]

$$C_c \frac{\partial T_c}{\partial t} = \nabla \cdot (\boldsymbol{\kappa_c} \nabla T_c) - G(T_c - T_l) + S$$

$$C_l \frac{\partial T_l}{\partial t} = \nabla \cdot (\boldsymbol{\kappa_l} \nabla T_l) + G(T_c - T_l)$$

$$C_s \frac{\partial T_s}{\partial t} = \kappa_s \nabla^2 T_s$$

With the boundary and initial conditions:

$$\kappa_{c,z} \frac{\partial T_c}{\partial z}\bigg|_{z=d} = -S_{cs}$$

$$\kappa_{l,z} \frac{\partial T_l}{\partial z}\bigg|_{z=d} = -S_{ls}$$

$$\kappa_s \frac{\partial T_s}{\partial z}\bigg|_{z=d} = S_{cs} + S_{ls}$$

where T_c, T_l, and T_s are the temperatures of the carrier, lattice, and substrate, respectively. G represents the carrier-phonon coupling. κ and C are the thermal conductivity and heat capacity of the carrier (κ_c, C_c), lattice (κ_l, C_l), and substrate (κ_s, C_s).

While the TTM provides a comprehensive theoretical framework, fully parameterizing this model requires precisely known, temperature-dependent variables, such as temperature-dependent electronic heat capacity and thermal conductivity. Because these parameters remain unestablished for these Mn-doped 2D RP samples, attempting a full TTM fit necessitates introducing multiple unconstrained variables, inevitably leading to arbitrary fitting artifacts. Therefore, to ensure mathematical rigor and prevent overparameterization, we analyze the spatiotemporal variance using the expanding-Gaussian model to extract an effective diffusivity. This method reliably captures the macroscopic transport behavior without relying on arbitrary fitting parameters, providing a mathematically robust, relative basis for comparing the influence of different spacer ligands (PEA vs. BA), which is the central objective of this work.

Furthermore, the apparent non-Gaussian shape of the time-zero profile, as shown in **Figure S7D**, arises fundamentally from the diffraction rings associated with the Airy disk point-spread function intrinsic to wide-field detection. In prior studies, it has been standard practice to fit only the central lobe of the spatial profile with a Gaussian function while excluding the outer diffraction rings, as also previously illustrated (**Figure S8A and 8B**).[10,11] Applying a 2D Gaussian function to our own data also yields residuals that are dominated by the diffraction-ring pattern, indicating that the apparent deviation from an ideal Gaussian mainly originates from the diffraction-induced "artifact" rather than from the actual carrier population itself, as shown in

Figure S8C. In addition, the heavy tail in the azimuthally averaged profile in **Figure S8D** is visually exaggerated by the limited plotting range of -2.5 to 2.5 μm. When the profile is displayed over the full spatial range (**Figure S9**), the initial population and the oscillatory residual after subtracting the Gaussian component are more clearly visible.

3.5 Theory for kinetic model of band-edge–to–Mn^{2+} energy transfer

Photoexcitation creates a band-edge exciton in the inorganic layer. In the undoped host, the BE state relaxes radiatively (k_r) and non-radiatively (k_{nr}). Upon Mn doping, an additional channel transfers the excitation to the Mn^{2+} $^4T_1$ state (k_{ET}), which then emits through the spin- and parity-forbidden $^4T_1 \rightarrow {}^6A_1$ transition with radiative and nonradiative rates k_r^{Mn} and k_{nr}^{Mn}. The effective BE lifetimes without (τ^{BE}) and with ($\tau^{BE\ with\ Mn}$) Mn are therefore:

$$\tau^{BE} = 1/(k_r + k_{nr})$$

$$\tau^{BE\ with\ Mn} = 1/(k_r + k_{nr} + k_{ET})$$

The BE decays are multi-exponential, $I(t) = \sum a_i \cdot exp(-t/\tau_i)$. Two averages are commonly reported:

$$\langle\tau\rangle_{amp} = \sum a_i\tau_i / \sum a_i \quad ; \quad \langle\tau\rangle_{int} = \sum a_i\tau_i^2 / \sum a_i\tau_i$$

Because the integrated emission is proportional to the area under the decay, $\sum a_i\tau_i$, the steady-state PLQY of a channel is set by the amplitude-weighted average, $PLQY_{BE} = k_r \cdot \langle\tau\rangle_{amp}$. We therefore use $\langle\tau\rangle_{amp}$ throughout; the intensity-weighted average (which is dominated by the longest-lived, lowest-population component) is not appropriate for yield-type quantities. The fits and the extracted averages are both listed in **Tables S5 and S6**.

With $PLQY_{BE} = k_r \cdot \langle\tau\rangle_{amp}$ and $\langle\tau\rangle^{BE}$ from the undoped fits, the host rate constants follow as

$$k_r = PLQY_{BE(undoped)}/\langle\tau\rangle^{BE}$$

and

$$k_{nr} = 1/\langle\tau\rangle^{BE} - k_r$$

The values (**Table S7**) are similar for the two spacers, consistent with their near-identical bandgap and band-edge emission and validate the assumption that k_r is unchanged upon doping.

The BE-to-Mn^{2+} transfer efficiency can be written equivalently from the lifetimes or, using $PLQY_{BE} = k_r \cdot \langle\tau\rangle_{amp}$ with constant k_r, from the steady-state BE quenching:

$$\Phi_{\mathrm{ET}} = 1 - \frac{\langle\tau\rangle^{BE\ with\ Mn}}{\langle\tau\rangle^{BE}} = 1 - \frac{PLQY_{BE\ with\ Mn}}{PLQY_{BE}}$$

For the Mn-doped PEA crystals, the BE lifetime ($\langle\tau\rangle^{BE\ with\ Mn} \approx 0.029$ ns) is shorter than the instrument response (FWHM ≈ 0.8 ns) and is therefore not quantitative; the lifetime route gives $\Phi_{ET} \approx 99\%$ only as an upper estimate. We consequently evaluate Φ_{ET} from the steady-state route, which is not instrument-limited, giving Φ_{ET} = 94% (PEA) and 51% (BA).

The measured Mn^{2+} PLQY is the product of the fraction of excitons delivered to Mn^{2+} (Φ_{ET}), and the fraction of those that emit radiatively (Φ_{Mn}):

$$PLQY_{Mn} = \Phi_{ET} \cdot \Phi_{Mn} \qquad \Longrightarrow \qquad \Phi_{Mn} = PLQY_{Mn}/\Phi_{ET}$$

With $PLQY_{Mn}$ = 45.9% (PEA) and 7.9% (BA) (Table S4), the intrinsic Mn^{2+} yield is Φ_{Mn} = 49% (PEA) and 15% (BA). The ~6-fold difference in Mn^{2+} PLQY is thus composed of a ~1.8-fold difference in transfer efficiency and a ~3.2-fold difference in intrinsic Mn^{2+} quantum yield.

The Mn^{2+} emission decay at 610 nm (**Figure 5C, Table S6**) gives amplitude-weighted lifetimes $\langle\tau\rangle^{Mn}$ of 467 µs (PEA) and 170 µs (BA). Since $\Phi_{Mn} = k_{r,Mn} \cdot \langle\tau\rangle^{Mn}$, the radiative lifetime is

$$\tau_{r,Mn} = \langle\tau\rangle^{Mn}/\Phi_{Mn}$$

which yields $\tau_{r,Mn}$ = 0.95 ms (PEA) and 1.1 ms (BA), equal within error and typical of the octahedral Mn^{2+} $^4T_1 \rightarrow {}^6A_1$ transition, confirming a lattice-independent $k_{r,Mn}$.[12–14] Because BA shows both a lower Φ_{Mn} and a shorter Mn^{2+} lifetime, the additional decay is non-radiative, consistent with faster multi-phonon relaxation in the softer, more strongly coupled BA lattice. A summary of the parameters used for and extracted by the kinetic model is shown in **Table S7**.

3.6 Density Functional Theory (DFT) calculations

First-principles calculations are based on DFT as implemented in the SIESTA package.[15,16] The nonlocal van der Waals density functional of Dion *et al*., corrected by Cooper (C09), to correctly describe the inorganic-organic interplay.[17,18] Geometry optimizations are performed with a spin-restricted formalism, while the band structures are described, including spin-orbit coupling through the so-called off-site approach following the Hemstreet formalism.[19] Core electrons are described with Troullier-Martins pseudopotentials, while valence wave functions are developed over a double-ζ polarized basis set of finite-range numerical pseudoatomic orbitals.[20,21] An energy cutoff of 150 Ry for the real-space mesh size has been used. The Brillouin zones are sampled using a 9×9×2 Γ-centered Monkhorst-Pack grid. Starting from the experimentally determined structure of both compounds, complete optimization of cell vectors and atomic positions is performed until forces are lower than 0.01 eV/Å. The Bulk modulus is determined by applying isotropic strains. The resulting variations of energy are fitted using the Murnaghan equation of states, leading to the value of the bulk modulus B_0.[22]

Section 2: Supplementary tables

Table S1. ICP-MS of $(PEA)_2Pb_{1-x}Mn_xBr_4$ ($x_{Mn,\ feed}$ = 0.50−0.90) crystals

Sample	Pb_{feed}	$x_{Mn,\ feed}$	Pb (%)	Mn (%) or *x* (%)
$(PEA)_2Pb_{1-x}Mn_xBr_4$ ($x_{Mn,\ feed}$ = 0.50)	0.50	0.50	99.930	0.070
$(PEA)_2Pb_{1-x}Mn_xBr_4$ ($x_{Mn,\ feed}$ = 0.70)	0.30	0.70	99.857	0.143
$(PEA)_2Pb_{1-x}Mn_xBr_4$ ($x_{Mn,\ feed}$ = 0.90)	0.10	0.90	99.708	0.292

Table S2. ICP-MS of $(BA)_2Pb_{1-x}Mn_xBr_4$ ($x_{Mn,\ feed}$ = 0.50−0.90) crystals

Sample	Pb_{feed}	$x_{Mn,\ feed}$	Pb (%)	Mn (%) or *x* (%)
$(BA)_2Pb_{1-x}Mn_xBr_4$ ($x_{Mn,\ feed}$ = 0.50)	0.50	0.50	99.930	0.031
$(BA)_2Pb_{1-x}Mn_xBr_4$ ($x_{Mn,\ feed}$ = 0.70)	0.30	0.70	99.857	0.079
$(BA)_2Pb_{1-x}Mn_xBr_4$ ($x_{Mn,\ feed}$ = 0.90)	0.10	0.90	99.687	0.313

Table S3. ICP-MS of $(L)_2Pb_{1-x}Mn_xBr_4$ (L= BzA or HA, $x_{Mn,feed}$ = 0.90) PCs

Sample	Pb_{feed}	$x_{Mn\ ,\ feed}$	Pb (%)	Mn (%) or *x* (%)
$(BzA)_2Pb_{1-x}Mn_xBr_4$ ($x_{Mn,feed}$ = 0.90)	0.10	0.90	99.50	0.50
$(HA)_2Pb_{1-x}Mn_xBr_4$ ($x_{Mn,feed}$ = 0.90)	0.10	0.90	99.81	0.19

Table S4. Spectrally resolved PLQY of undoped and doped samples.

Sample	BE PLQY (%)	Mn^{2+} PLQY (%)	Total PLQY (%)
$(PEA)_2PbBr_4$	15.00	-	15.00
$(PEA)_2Pb_{1-x}Mn_xBr_4$ (x = 0.0029)	0.97	45.90	46.90
$(BA)_2PbBr_4$	13.72	-	13.72
$(BA)_2Pb_{1-x}Mn_xBr_4$ (x = 0.0030)	6.71	7.91	14.62
$(BzA)_2PbBr_4$	5.75	-	5.75
$(BzA)_2Pb_{1-x}Mn_xBr_4$ (x = 0.0050)	0.91	21.11	22.01
$(HA)_2PbBr_4$	3.88	-	3.88
$(HA)_2Pb_{1-x}Mn_xBr_4$ (x = 0.0020)	2.78	1.33	4.11

Table S5. Fitting parameters for band edge PL decay of undoped and doped samples

Sample	τ_1 (ns)	A_1 (%)	τ_2 (ns)	A_2 (%)	τ_3 (ns)	A_3 (%)	$\langle\tau\rangle_{amp}$ (ns)	$\langle\tau\rangle_{int}$ (ns)
$(PEA)_2PbBr_4$	0.36	55	6.74	43	23.75	3	3.69	9.32
$(PEA)_2Pb_{1-x}Mn_xBr_4$ (x = 0.0029)	0.02	99	1.66	1			0.029	0.19
$(BA)_2PbBr_4$	1.97	49	6.53	49	28.562	2	4.73	8.22
$(BA)_2Pb_{1-x}Mn_xBr_4$ (x = 0.0030)	0.78	63	2.79	36	13.29	1	1.62	3.01
$(BzA)_2PbBr_4$	1.56	57	6.16	40	21.43	3	3.99	7.37
$(BzA)_2Pb_{1-x}Mn_xBr_4$ (x = 0.0050)	0.1	99	3.67	1			0.136	0.75
$(HA)_2PbBr_4$	1.11	70	4.00	29	22.75	1	2.16	5.58
$(HA)_2Pb_{1-x}Mn_xBr_4$ (x = 0.0020)	0.58	66	2.47	33	16.28	1	1.36	3.52

Table S6. Fitting parameters for Mn^{2+} emission decay measured at 610 nm.

Sample	τ_1 (μs)	A_1 (%)	τ_2 (μs)	A_2 (%)	τ_3 (μs)	A_3 (%)	$\langle\tau\rangle_{amp}$ (μs)	$\langle\tau\rangle_{int}$ (μs)
$(PEA)_2Pb_{1-x}Mn_xBr_4$ (x = 0.0029)	50.2	9	252	24	602	67	467	551
$(BA)_2Pb_{1-x}Mn_xBr_4$ (x = 0.0030)	8.92	57	103	19	610	24	170	533

Table S7. Parameters of the BE-to-Mn^{2+} kinetic model for $(PEA)_2PbBr_4$ and $(BA)_2PbBr_4$ (for doped samples $x \approx 0.3\%$). Amplitude-weighted averaged lifetimes are used as discussed.

Quantity	Symbol	PEA	BA
BE lifetime, undoped (ns)	$\langle\tau\rangle^{BE}$	3.69	4.73
BE lifetime, doped (ns)	$\langle\tau\rangle^{BE\ with\ Mn}$	0.029	1.62
BE radiative rate (ns^{-1})	k_r	0.041	0.029
BE non-radiative rate (ns^{-1})	k_{nr}	0.23	0.18
BE PLQY, undoped (%)	$PLQY_{BE}$	15	14
BE PLQY, doped (%)	$PLQY_{BE\ with\ Mn}$	0.97	6.71
Mn^{2+} PLQY, doped (%)	$PLQY_{Mn}$	45.9	7.9
Energy-transfer efficiency (%)	Φ_{ET}	94	51
Intrinsic Mn^{2+} quantum yield (%)	Φ_{Mn}	49	15.5
Mn^{2+} lifetime (μs)	$\langle\tau\rangle^{Mn}$	467	170
Mn^{2+} radiative lifetime (ms)	$\tau_{r,Mn}$	0.95	1.1
Mn^{2+} non-radiative rate (μs^{-1})	$k_{nr,Mn}$	$1.1 \cdot 10^{-3}$	$4.9 \cdot 10^{-3}$

Section 3: Supplementary Figures

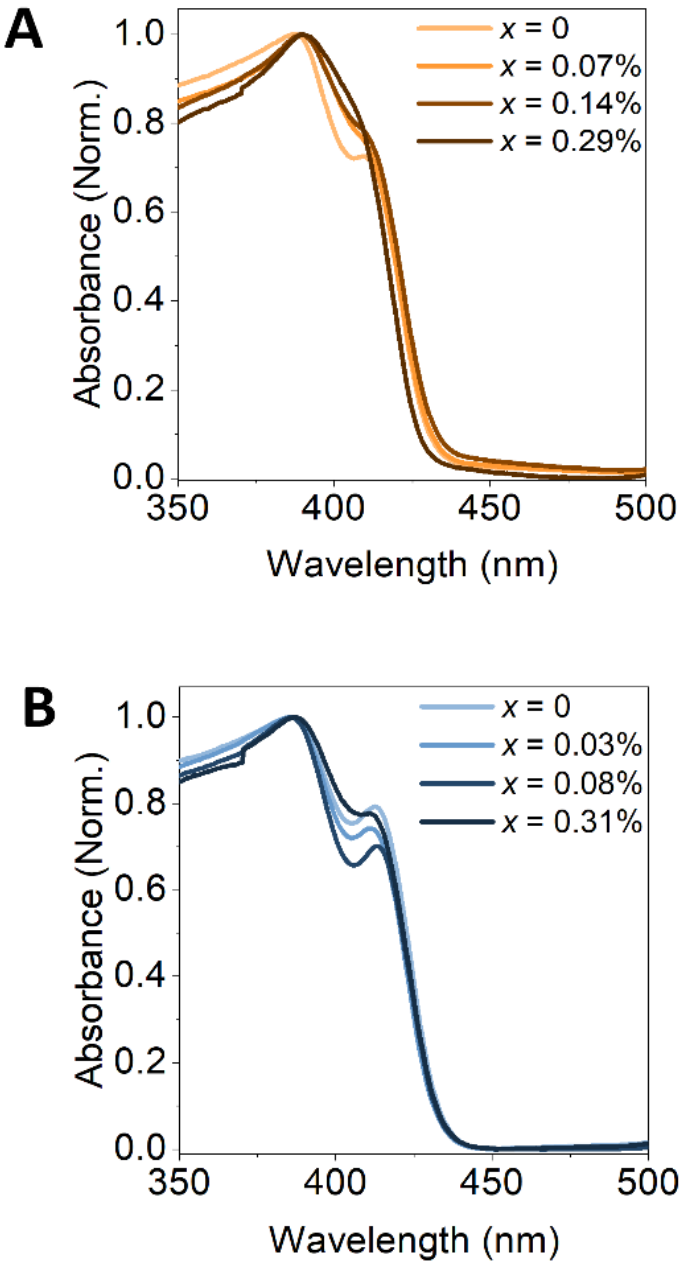

Figure S1. Absorption spectra of (A) $(PEA)_2Pb_{1-x}Mn_xBr_4$ and (B) $(BA)_2Pb_{1-x}Mn_xBr_4$ perovskite crystals, with x varying from 0 to 0.29% for PEA and from 0 to 0.31% for BA.

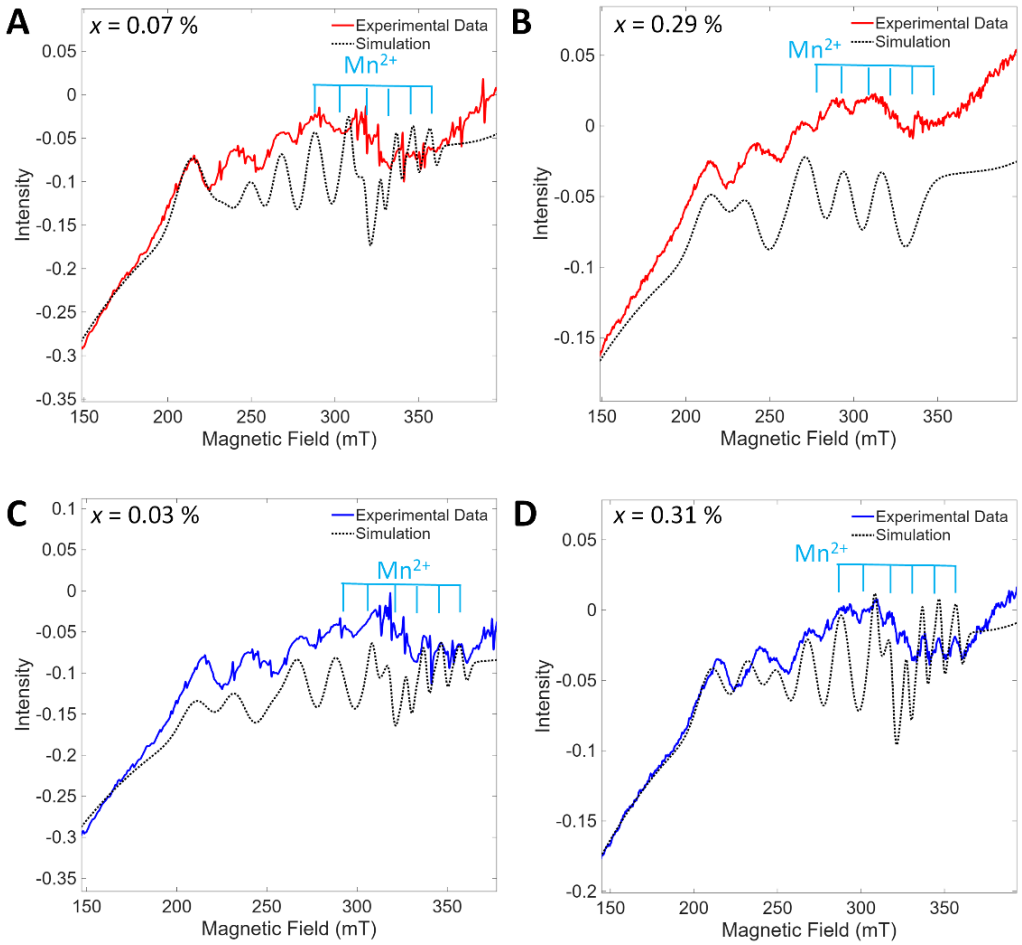

Figure S2. (A, B) EPR spectra and simulations of $(PEA)_2Pb_{1-x}Mn_xBr_4$ bulk crystals at x = 0.06% (A) and 0.29% (B). (C-D) EPR spectra and simulations of $(BA)_2Pb_{1-x}Mn_xBr_4$ bulk crystals at x = 0.03%(C) and 0.31% (D).

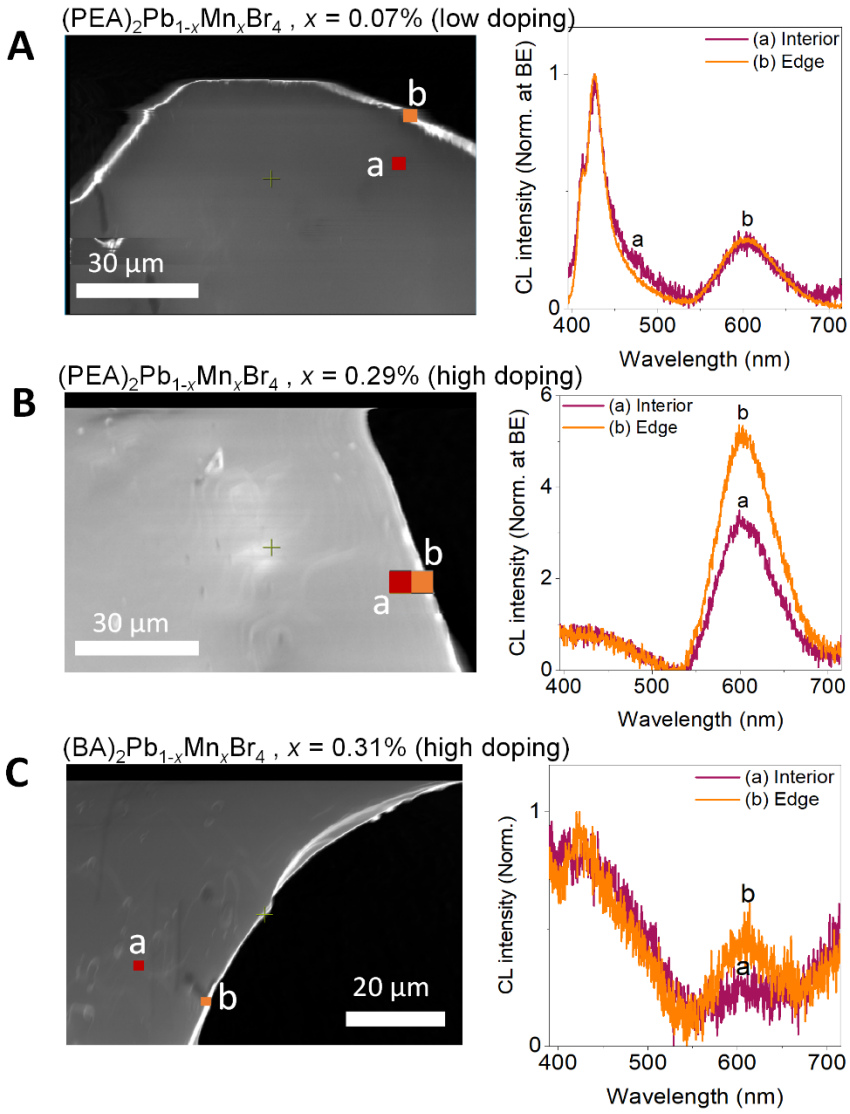

Figure S3. (A, B) FE-SEM image (left) and CL spectra (right) of $(PEA)_2Pb_{1-x}Mn_xBr_4$ bulk crystals at low doping (x = 0.07%) (A), and high doping (x = 0.29%) (B). (C) FE-SEM image (left) and CL spectra (right) of $(BA)_2Pb_{1-x}Mn_xBr_4$ crystals at high doping (x = 0.31%).

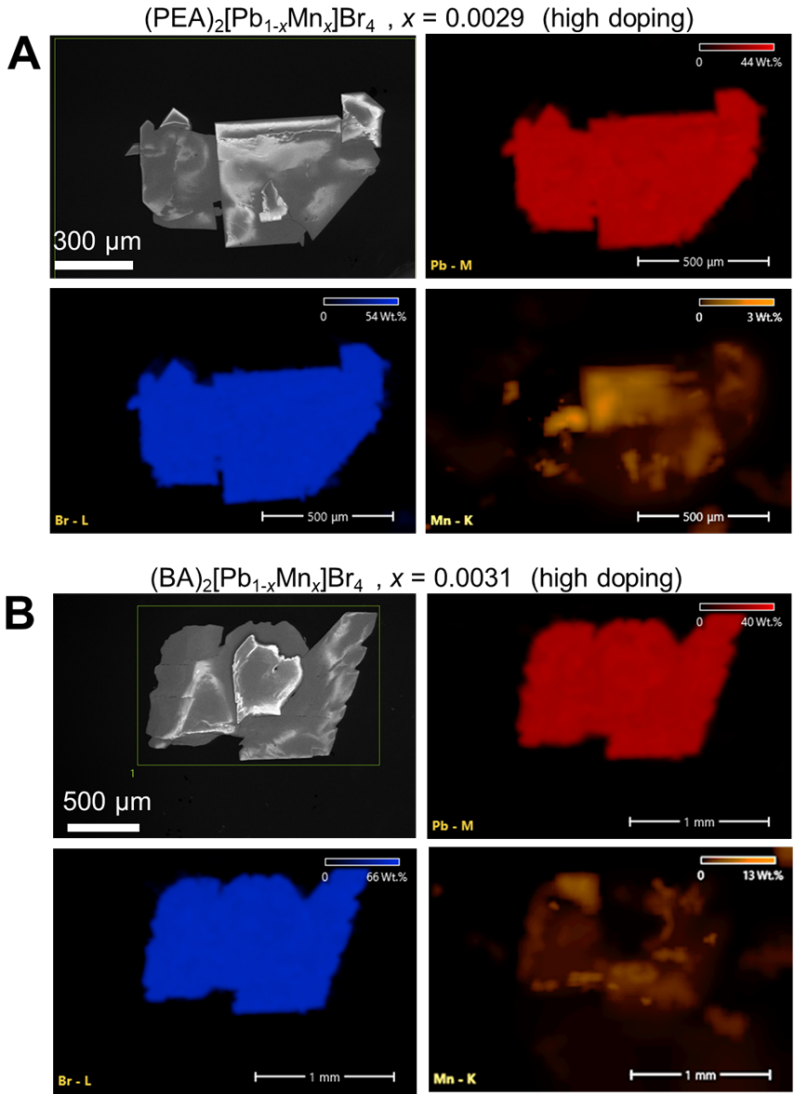

Figure S4. SEM images with EDS elemental mapping of highly Mn-doped crystals. (A) $(PEA)_2Pb_{1-x}Mn_xBr_4$ ($x = 0.0029$ or 0.29%). (B) $(BA)_2Pb_{1-x}Mn_xBr_4$ ($x = 0.0031$ or 0.31%). The maps show the spatial distribution of Pb (red), Br (blue), and Mn (yellow).

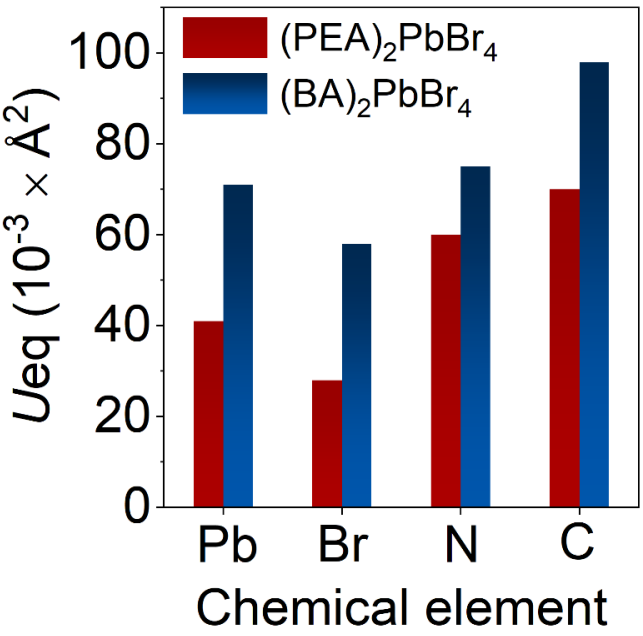

Figure S5. Atomic displacement of Pb, Br, N, and C in $(PEA)_2PbBr_4$ and $(BA)_2PbBr_4$ perovskites derived from single-crystal XRD.[23]

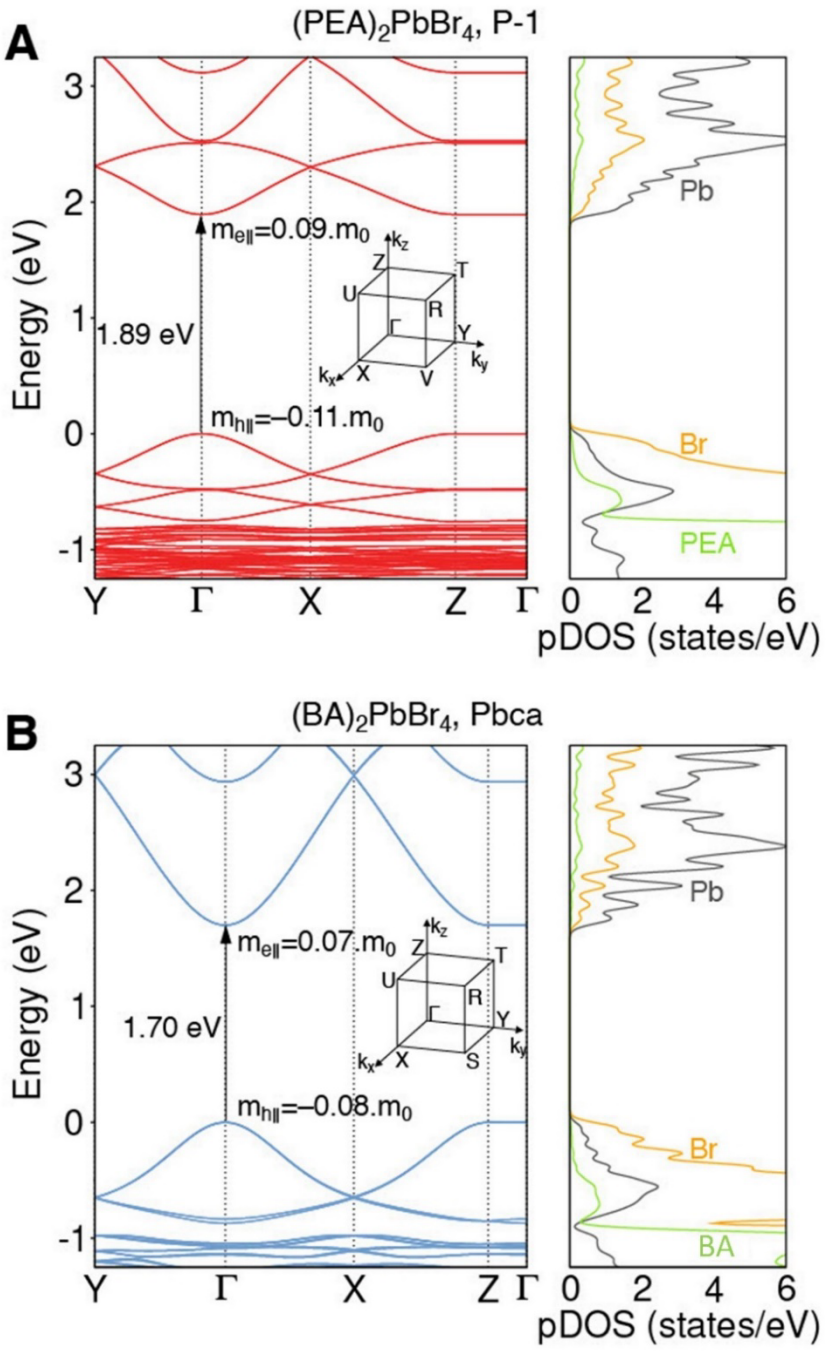

Figure S6. Density functional theory (DFT) computed band structure of (A) $(PEA)_2PbBr_4$ and (B) $(BA)_2PbBr_4$. The right panel of the Figures shows the respective partial density of states (pDOS).

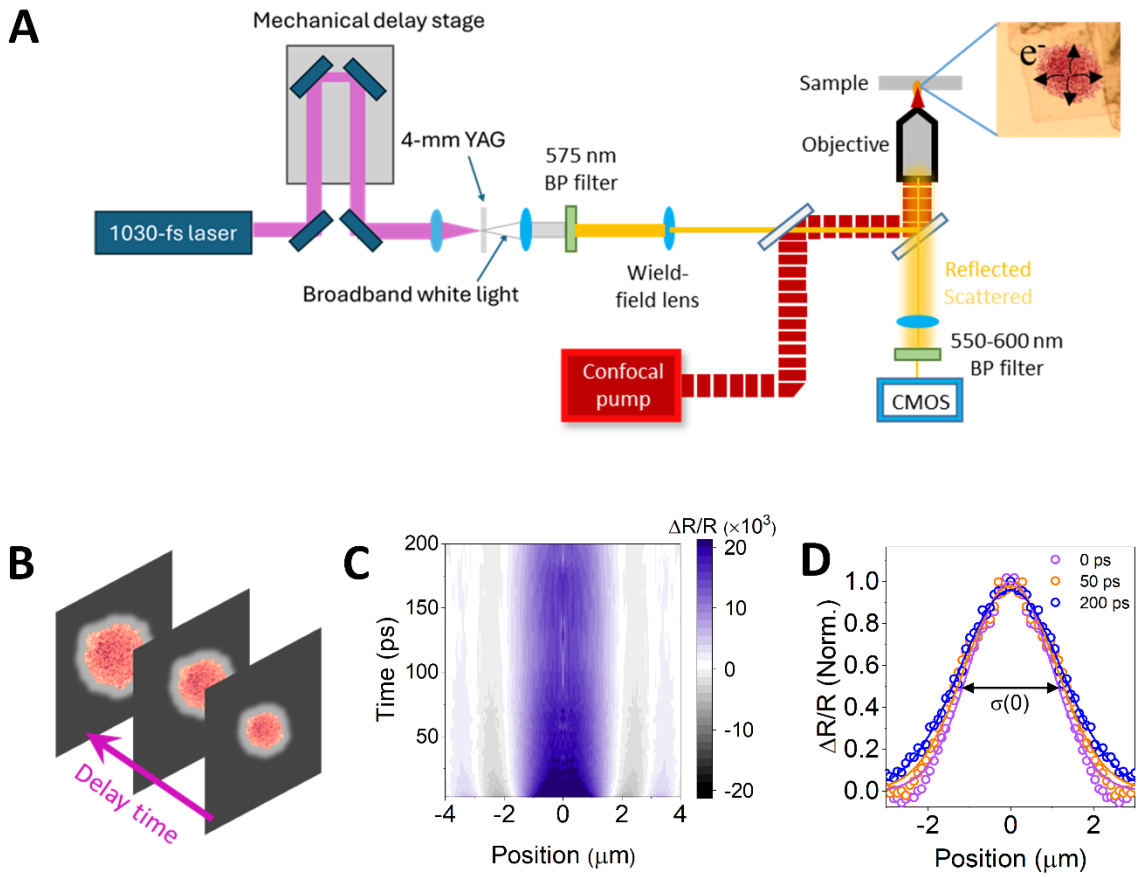

Figure S7. (A) Schematic representation of the experimental setup for pump–probe transient reflection microscopy. (B) Schematic representation of exciton diffusion as a function of pump-probe time delay at the CMOS camera. (C) Diffusion map of the $(BA)_2PbBr_4$ crystal, highlighting the spatial spreading of excitons. In Figure C, the spatio-temporal profiles are directly constructed from the azimuthally averaged data by symmetric duplication about $x = 0$ (D) Gaussian profiles extracted at different pump–probe delays (0, 50, and 200 ps); the mean square displacement (MSD) of the exciton population over time is calculated from these profiles.

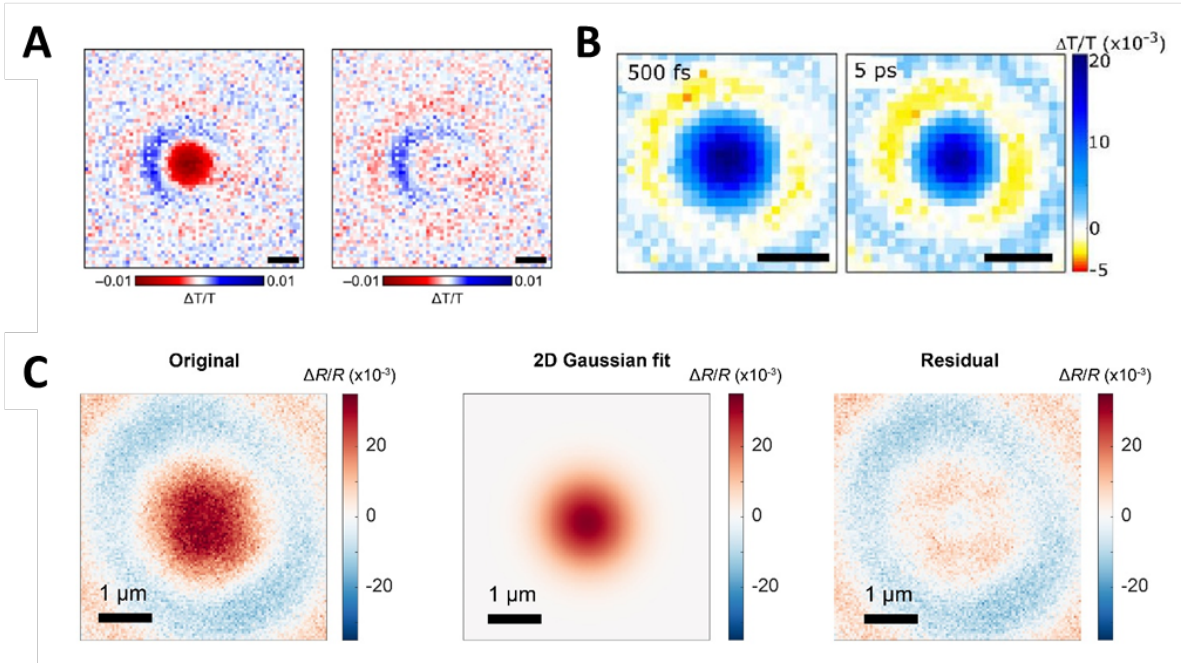

Figure S8. Wide-field transient imaging of pentacene films (used from ref. [10]). The left panel shows the original data, and the right panel displays the fitting residual after applying a 2D Gaussian fit. (B) Wide-field transient imaging of $MAPbI_3$ films at different delay times (500 fs, left; 5 ps, right) (used from ref. [11]). (C) Wide-field transient imaging of $(BA)_2PbBr_4$ (left panel), the corresponding fitted 2D Gaussian distribution (middle panel), and the fitting residual map (right panel) in this work.

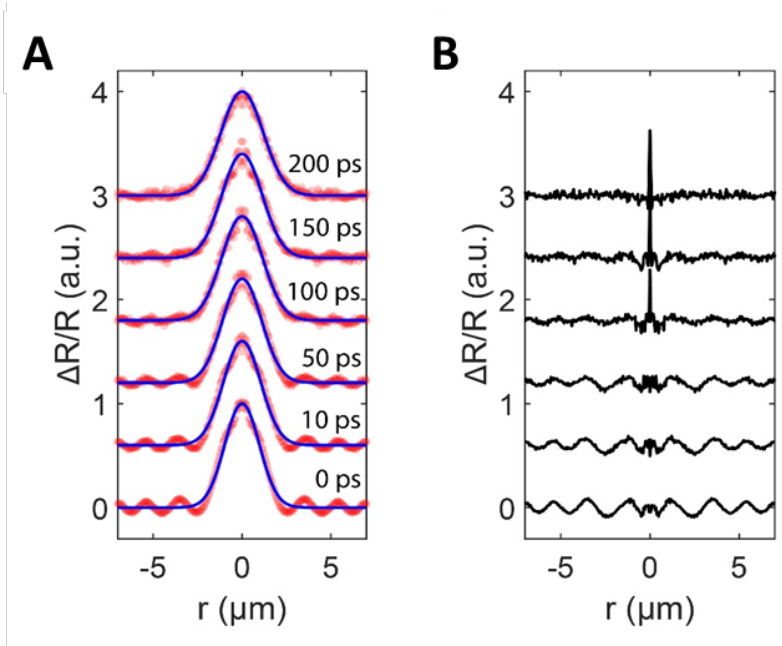

Figure S9. (A) Experimentally measured (red dots) and Gaussian-fitted (blue lines) profiles of the excitons at various delay times for $(BA)_2PbBr_4$. (B) The fitting residuals of (A) exhibit pure diffraction-induced oscillations.

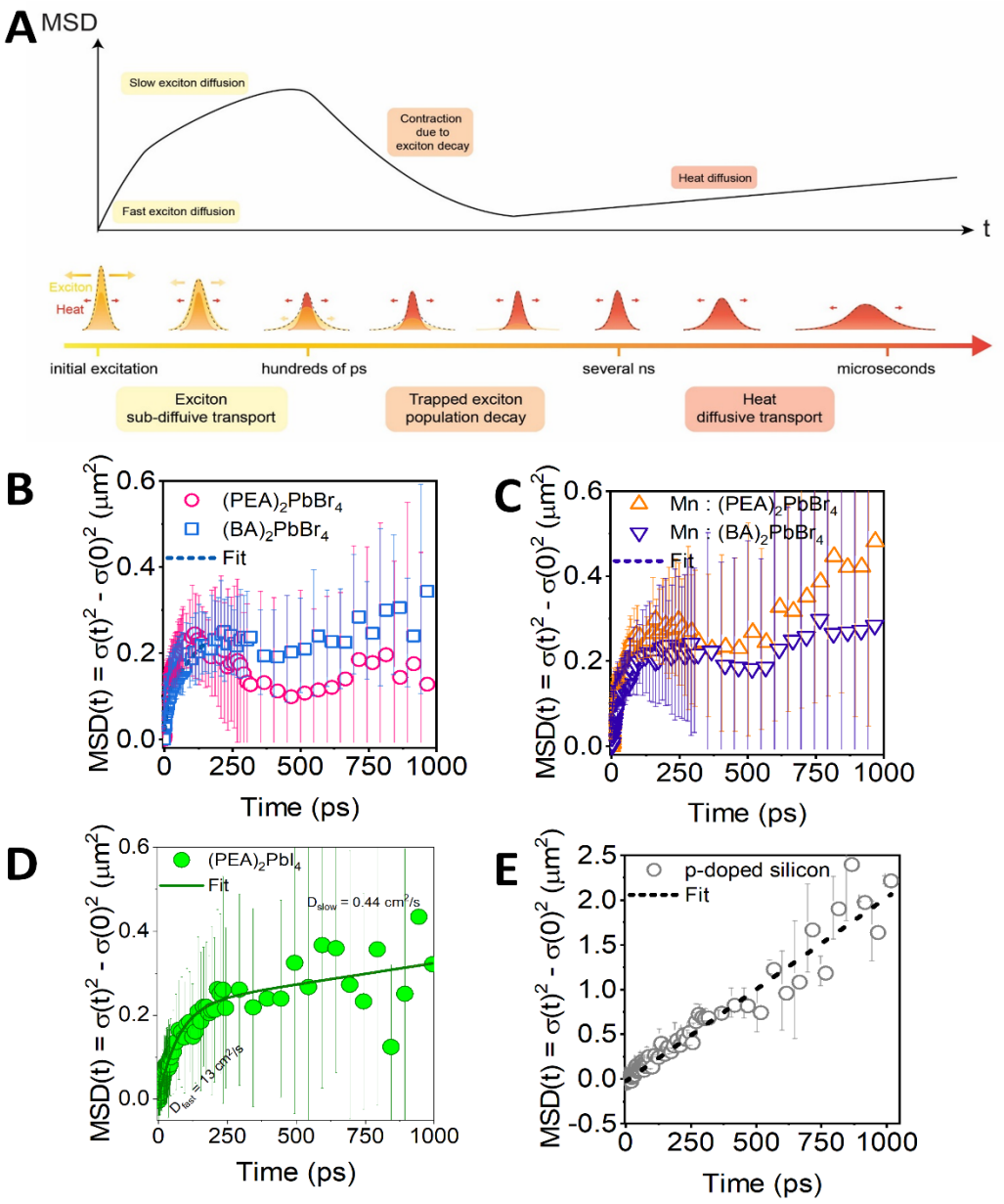

Figure S10. (A) Schematic representation of events occurring in the MSD *vs* time plot for Br-based perovskites. At early times, the MSD is expanded due to hot carriers and exciton diffusion. This is followed by an apparent ("artificial") contraction at longer delay times as the excitonic contribution diminishes and the slowly-diffusing heat starts to affect the TRM contrast. At the nanosecond scale and longer times, the heat will be the predominant diffusing species. (B, C) MSD *vs* time plot of undoped and Mn-doped L_2PbBr_4 (L = PEA or BA) crystals in a longer time scale. (D, E) MSD *vs* time plot of $(PEA)_2PbI_4$ perovskites (D) and standard p-doped silicon (E).

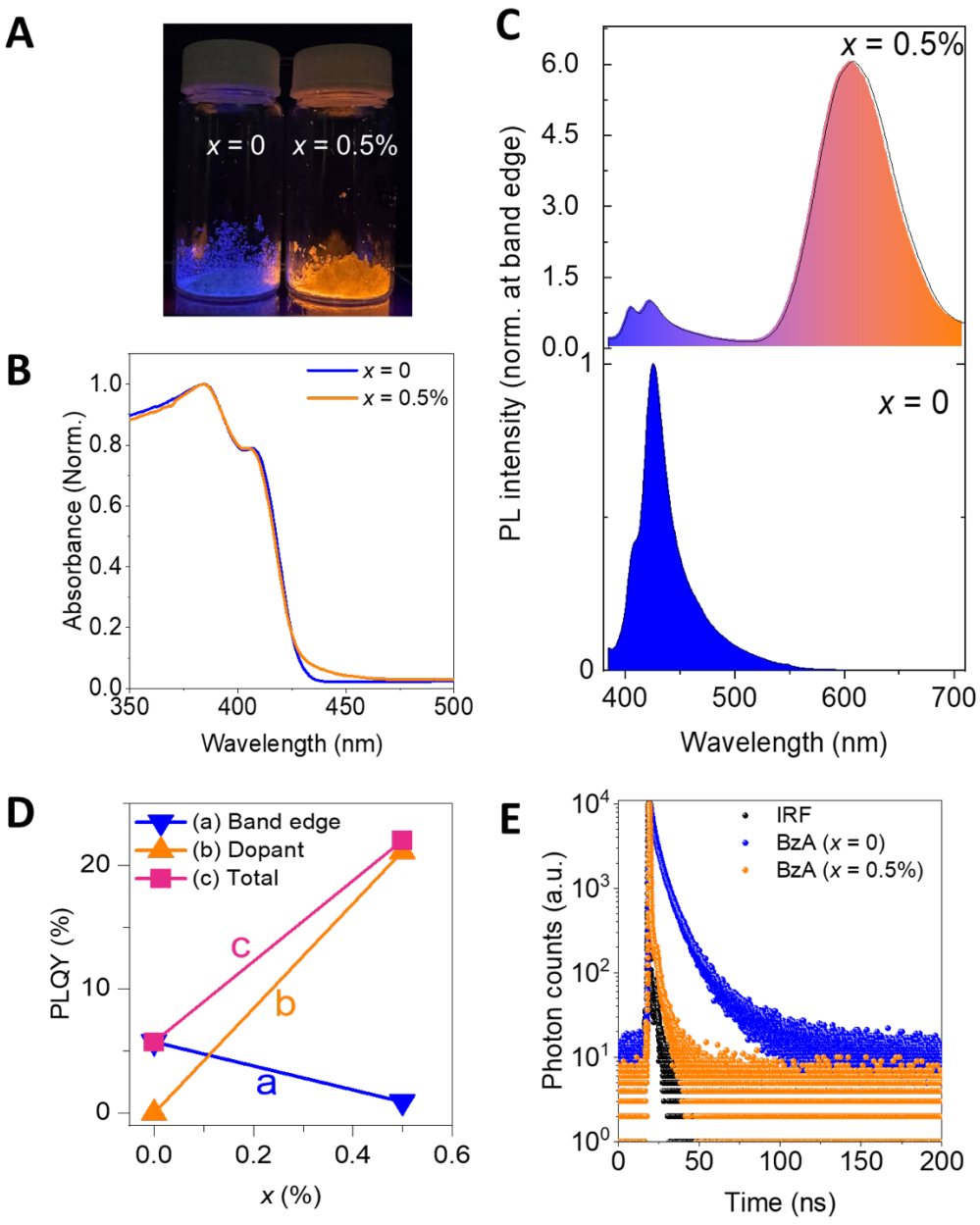

Figure S11. (A) Photographs of $(BzA)_2Pb_{1-x}Mn_xBr_4$ (x = 0, 0.5%) perovskites under UV (365 nm). (B-E) Absorption (B), PL spectra (C), PLQYs (D), and PL decays (E) of $(BzA)_2Pb_{1-x}Mn_xBr_4$ crystals (x = 0, 0.5%).

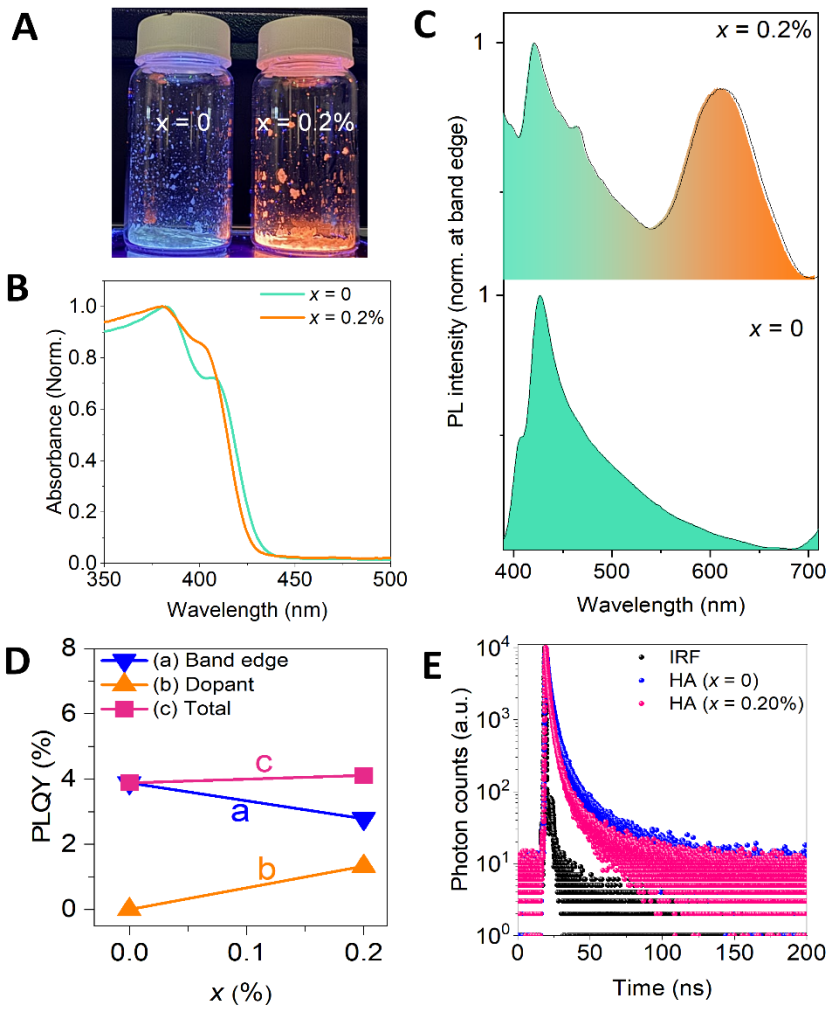

Figure S12. (A) Photographs of $(HA)_2Pb_{1-x}Mn_xBr_4$ (x = 0, 0.2%) perovskites under UV (365 nm). (B-E) Absorption (B), PL spectra (C), PLQYs (D), and PL decays (E) of $(HA)_2Pb_{1-x}Mn_xBr_4$ bulk crystals (x = 0, 0.2%).

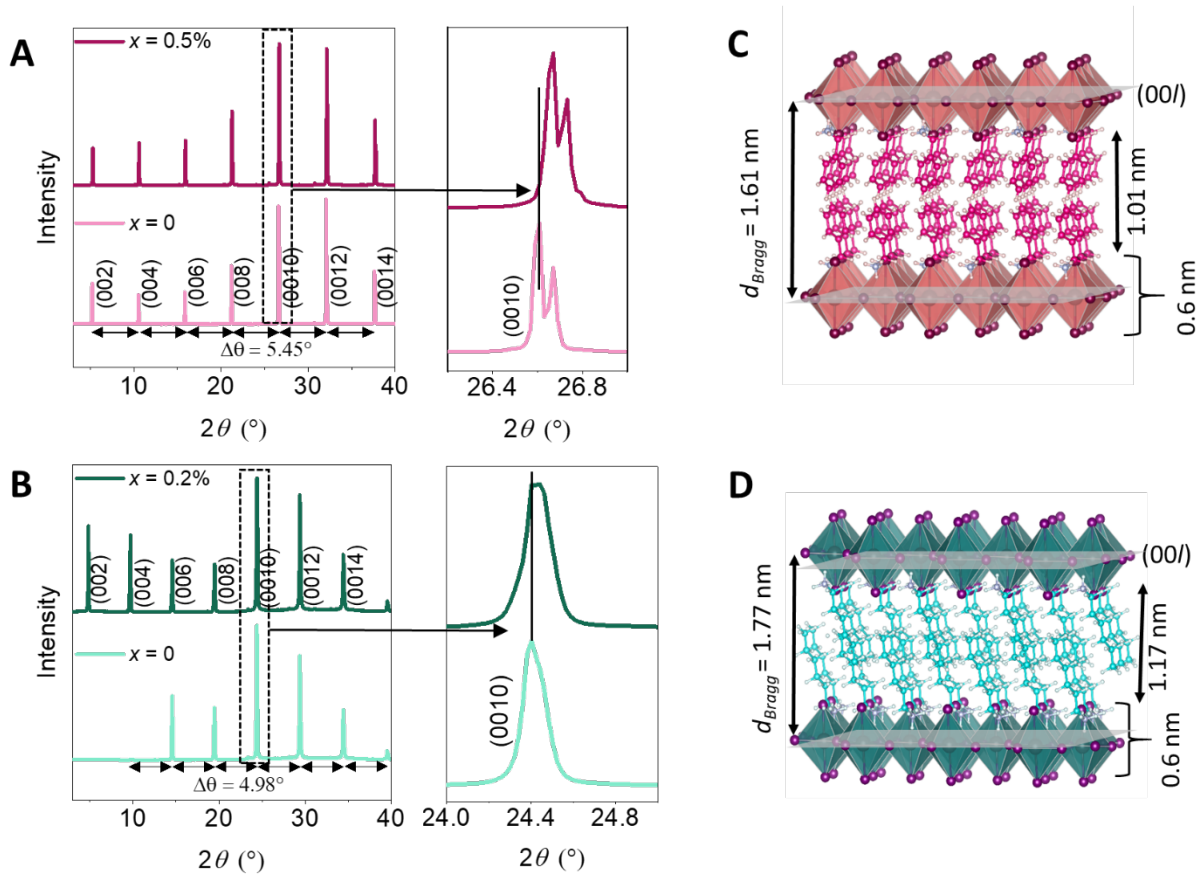

Figure S13. (A, B) pXRD patterns of (A) $(BzA)_2Pb_{1-x}Mn_xBr_4$ and (B) $(HA)_2Pb_{1-x}Mn_xBr_4$ bulk crystals, where x = 0, 0.5% (BzA), and 0.2% (HA). The right panels of the figure show the shifting of the (0010) plane towards a higher angle with doping. (C, D) Schematic diagram of the crystal structure of (C) $(BzA)_2PbBr_4$ and (D) $(HA)_2PbBr_4$ perovskites, where the length of spacer ligands was calculated using the periodicity of the diffraction planes. The Vesta software is used to draw these structures using their CIF files.

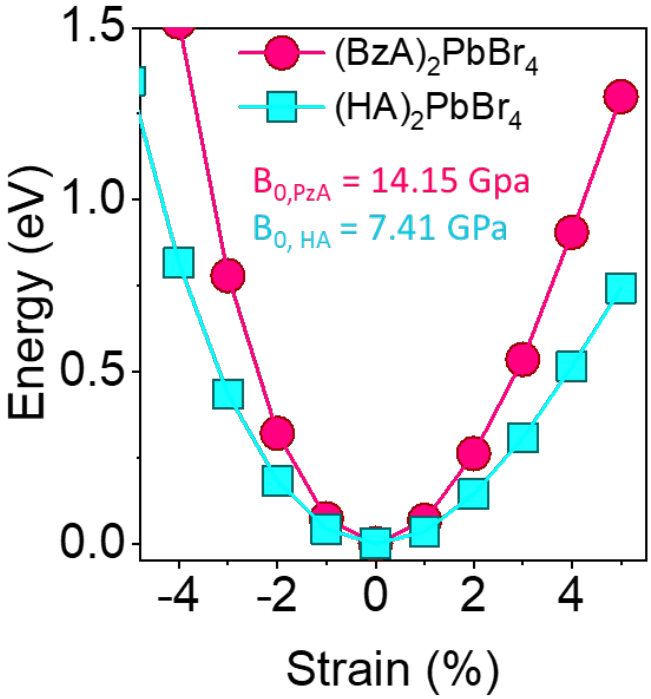

Figure S14. Energy *versus* strain plot of $(BzA)_2PbBr_4$ and $(HA)_2PbBr_4$ for the evaluation of the Bulk modulus.

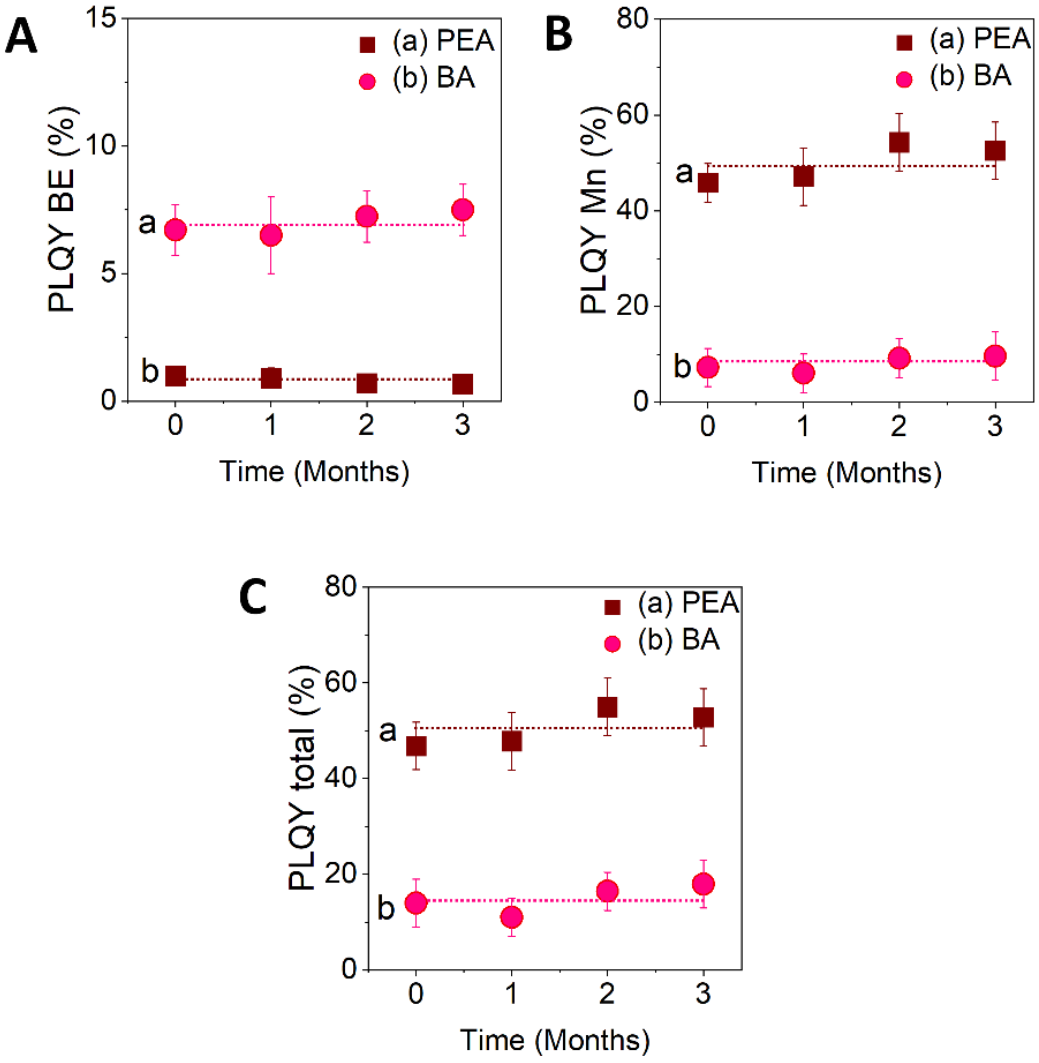

Figure S15. (A-F) Evolution of PLQY of Mn (~0.3%) doped L_2PbBr_4 (L =PEA or BA) bulk crystals with time, (A) at band edge peak (BE), (B) at Mn peak, and (C) total (BE + Mn peaks).

Section 4: References for SI.

(1) Stoumpos, C. C.; Cao, D. H.; Clark, D. J.; Young, J.; Rondinelli, J. M.; Jang, J. I.; Hupp, J. T.; Kanatzidis, M. G. Ruddlesden-Popper Hybrid Lead Iodide Perovskite 2D Homologous Semiconductors. *Chem. Mater.* **2016**, *28* (8), 2852–2867. https://doi.org/10.1021/acs.chemmater.6b00847.

(2) Dutta, T.; Kashid, S. M.; Hooda, R.; Sheikh, T.; Chowdhury, A.; Nag, A. Edge versus Interior Mn 2+ Doping in 2D Layered Butylammonium Lead Bromide Perovskite Single Crystals. *J. Phys. Chem. C* **2022**, *126* (49), 21109–21116. https://doi.org/10.1021/acs.jpcc.2c06911.

(3) Delor, M.; Weaver, H. L.; Yu, Q.; Ginsberg, N. S. Imaging Material Functionality through Three-Dimensional Nanoscale Tracking of Energy Flow. *Nat. Mater.* **2020**, *19* (1), 56–62. https://doi.org/10.1038/s41563-019-0498-x.

(4) Tulyagankhodjaev, J. A.; Shih, P.; Yu, J.; Russell, J. C.; Chica, D. G.; Reynoso, M. E.; Su, H.; Stenor, A. C.; Roy, X.; Berkelbach, T. C.; Delor, M. Room-Temperature Wavelike Exciton Transport in a van Der Waals Superatomic Semiconductor. *Science (80-.).* **2023**, *382* (6669), 438–442. https://doi.org/10.1126/science.adf2698.

(5) Seitz, M.; Magdaleno, A. J.; Alcázar-Cano, N.; Meléndez, M.; Lubbers, T. J.; Walraven, S. W.; Pakdel, S.; Prada, E.; Delgado-Buscalioni, R.; Prins, F. Exciton Diffusion in Two-Dimensional Metal-Halide Perovskites. *Nat. Commun.* **2020**, *11* (1), 1–8. https://doi.org/10.1038/s41467-020-15882-w.

(6) Block, A.; Liebel, M.; Yu, R.; Spector, M.; Sivan, Y.; García de Abajo, F. J.; van Hulst, N. F. Tracking Ultrafast Hot-Electron Diffusion in Space and Time by Ultrafast Thermomodulation Microscopy. *Sci. Adv.* **2019**, *5* (5). https://doi.org/10.1126/sciadv.aav8965.

(7) Liu, Q.; Wei, K.; Tang, Y.; Xu, Z.; Cheng, X.; Jiang, T. Visualizing Hot-Carrier Expansion and Cascaded Transport in WS 2 by Ultrafast Transient Absorption Microscopy. *Adv. Sci.* **2022**, *9* (10). https://doi.org/10.1002/advs.202105746.

(8) Carwithen, B. P.; Hopper, T. R.; Ge, Z.; Mondal, N.; Wang, T.; Mazlumian, R.; Zheng, X.; Krieg, F.; Montanarella, F.; Nedelcu, G.; Kroll, M.; Siguan, M. A.; Frost, J. M.; Leo, K.; Vaynzof, Y.; Bodnarchuk, M. I.; Kovalenko, M. V.; Bakulin, A. A. Confinement and

Exciton Binding Energy Effects on Hot Carrier Cooling in Lead Halide Perovskite Nanomaterials. *ACS Nano* **2023**, *17* (7), 6638–6648. https://doi.org/10.1021/acsnano.2c12373.

(9) Deng, S.; Shi, E.; Yuan, L.; Jin, L.; Dou, L.; Huang, L. Long-Range Exciton Transport and Slow Annihilation in Two-Dimensional Hybrid Perovskites. *Nat. Commun.* **2020**, *11* (1), 664. https://doi.org/10.1038/s41467-020-14403-z.

(10) Schnedermann, C.; Sung, J.; Pandya, R.; Verma, S. D.; Chen, R. Y. S.; Gauriot, N.; Bretscher, H. M.; Kukura, P.; Rao, A. Ultrafast Tracking of Exciton and Charge Carrier Transport in Optoelectronic Materials on the Nanometer Scale. *J. Phys. Chem. Lett.* **2019**, *10* (21), 6727–6733. https://doi.org/10.1021/acs.jpclett.9b02437.

(11) Sung, J.; Schnedermann, C.; Ni, L.; Sadhanala, A.; Chen, R. Y. S.; Cho, C.; Priest, L.; Lim, J. M.; Kim, H.-K.; Monserrat, B.; Kukura, P.; Rao, A. Long-Range Ballistic Propagation of Carriers in Methylammonium Lead Iodide Perovskite Thin Films. *Nat. Phys.* **2020**, *16* (2), 171–176. https://doi.org/10.1038/s41567-019-0730-2.

(12) Ji, S.; Liu, Z.; Zhao, L.; Zhao, K.; Tan, H.; Wang, J.; Zhao, J.; Zheng, J.; Yuan, X. Controlled Photoluminescence Lifetimes and Quantum Efficiencies in Mn-Doped Two-Dimensional Perovskite via A-Site Cation Engineering. *J. Phys. Chem. C* **2023**, *127* (43), 21313–21320. https://doi.org/10.1021/acs.jpcc.3c04461.

(13) Li, S.; Jiang, J.; Zhang, H.; Fu, H.; Liu, J.; Song, Y.; Cao, S.; Yang, W.; Zheng, J.; Zhao, J. Luminescence Properties of Mn-Doped 2D Organic-Inorganic Hybrid Perovskites: Insights from (PPA)2PbBr4 Perovskite. *Mater. Res. Bull.* **2024**, *170*, 112568. https://doi.org/10.1016/j.materresbull.2023.112568.

(14) Su, B.; Molokeev, M. S.; Xia, Z. Unveiling Mn 2+ Dopant States in Two-Dimensional Halide Perovskite toward Highly Efficient Photoluminescence. *J. Phys. Chem. Lett.* **2020**, *11* (7), 2510–2517. https://doi.org/10.1021/acs.jpclett.0c00593.

(15) Soler, J. M.; Artacho, E.; Gale, J. D.; García, A.; Junquera, J.; Ordejón, P.; Sánchez-Portal, D. The SIESTA Method for Ab Initio Order- N Materials Simulation. *J. Phys. Condens. Matter* **2002**, *14* (11), 2745–2779. https://doi.org/10.1088/0953-8984/14/11/302.

(16) García, A.; Papior, N.; Akhtar, A.; Artacho, E.; Blum, V.; Bosoni, E.; Brandimarte, P.; Brandbyge, M.; Cerdá, J. I.; Corsetti, F.; Cuadrado, R.; Dikan, V.; Ferrer, J.; Gale, J.; García-Fernández, P.; García-Suárez, V. M.; García, S.; Huhs, G.; Illera, S.; Korytár, R.;

Koval, P.; Lebedeva, I.; Lin, L.; López-Tarifa, P.; Mayo, S. G.; Mohr, S.; Ordejón, P.; Postnikov, A.; Pouillon, Y.; Pruneda, M.; Robles, R.; Sánchez-Portal, D.; Soler, J. M.; Ullah, R.; Yu, V. W.; Junquera, J. S SIESTA : Recent Developments and Applications. *J. Chem. Phys.* **2020**, *152* (20). https://doi.org/10.1063/5.0005077.

(17) Dion, M.; Rydberg, H.; Schröder, E.; Langreth, D. C.; Lundqvist, B. I. Van Der Waals Density Functional for General Geometries. *Phys. Rev. Lett.* **2004**, *92* (24), 246401. https://doi.org/10.1103/PhysRevLett.92.246401.

(18) Cooper, V. R. Van Der Waals Density Functional: An Appropriate Exchange Functional. *Phys. Rev. B* **2010**, *81* (16), 161104. https://doi.org/10.1103/PhysRevB.81.161104.

(19) Cuadrado, R.; Cerdá, J. I. Fully Relativistic Pseudopotential Formalism under an Atomic Orbital Basis: Spin–Orbit Splittings and Magnetic Anisotropies. *J. Phys. Condens. Matter* **2012**, *24* (8), 086005. https://doi.org/10.1088/0953-8984/24/8/086005.

(20) Troullier, N.; Martins, J. L. Efficient Pseudopotentials for Plane-Wave Calculations. *Phys. Rev. B* **1991**, *43* (3), 1993–2006. https://doi.org/10.1103/PhysRevB.43.1993.

(21) Artacho, E., Sánchez-Portal, D., Ordejón, P., García, A. & Soler, J. M. Linear-Scaling Ab-Initio Calculations for Large and Complex Systems. *Phys. status solidi* **1999**, *215* (1), 809–817. https://doi.org/10.1002/(SICI)1521-3951(199909)215:1<809::AID-PSSB809>3.0.CO;2-0.

(22) Murnaghan, F. D. The Compressibility of Media under Extreme Pressures. *Proc. Natl. Acad. Sci.* **1944**, *30* (9), 244–247. https://doi.org/10.1073/pnas.30.9.244.

(23) Gong, X.; Voznyy, O.; Jain, A.; Liu, W.; Sabatini, R.; Piontkowski, Z.; Walters, G.; Bappi, G.; Nokhrin, S.; Bushuyev, O.; Yuan, M.; Comin, R.; McCamant, D.; Kelley, S. O.; Sargent, E. H. Electron–Phonon Interaction in Efficient Perovskite Blue Emitters. *Nat. Mater.* **2018**, *17* (6), 550–556. https://doi.org/10.1038/s41563-018-0081-x.